



Self-constructed facet junctions on hexagonal CdS single crystals with high photoactivity and photostability for water splitting

Xuqiang Hao^{a,b}, Yue Hu^{a,b}, Zhiwei Cui^{a,b}, Jun Zhou^{a,b}, Ying Wang^{a,b,*}, Zhigang Zou^b

^a School of Chemistry and Chemical Engineering, Nanjing University, Nanjing, 210023, PR China

^b Eco-materials and Renewable Energy Research Center (ERERC), National Laboratory of Solid State Microstructures, Kunshan Innovation Institute of Nanjing University, Jiangsu Key Laboratory for Nanotechnology, Nanjing, 210023, PR China



ARTICLE INFO

Keywords:

Hexagonal CdS single crystals
{0001} facets
Facet junction
Photocatalytic hydrogen evolution

ABSTRACT

Crystal facets engineering of semiconductor catalysts with different exposed facets has been proven as a versatile approach to enhance their photocatalytic performance. Herein, for the first time, a facet-junction engineered hexagonal CdS single crystal with exposing {0001} and {1010} facets was synthesized by hydrothermal reaction via adjusting the molar ratio of S²⁻/Cd²⁺ precursor. The co-exposed {0001} and {1010} facets on hexagonal CdS single crystals with continuous band bending and well-defined epitaxial interfaces showed highly efficient visible-light-induced H₂ evolution. The maximum photocatalytic H₂ production rate of 24.33 mmol h⁻¹ g⁻¹ is obtained over the facet-junction engineered hexagonal CdS-5 single crystals with an apparent quantum efficiency of 11.18% at 470 nm, which is about 5.27 times greater than CdS-1 nanoparticles. Also, superior photostability is also achieved, even after 25 consecutive cycles during 100 h light irradiation keeping impregnated in strong alkaline sacrificial agent beyond 20 days, the initial photoactivity is still remained. The enhanced photocatalytic H₂ evolution activity and photostability can be ascribed to the type-II band alignment between the co-exposed {0001} and {1010} facets that significantly promoted the separation rate of photo-generated electrons and holes. And the small amount of sulfur vacancies are also benefit for the photocatalytic hydrogen evolution activity of CdS-5. The time-resolved fluorescence (TRPL) decay and photoelectrochemical test further proved the effective spatial charge separation. This work provides a feasible and simple strategy for designing of facet-junction engineered CdS single crystals with highly efficient photocatalytic activity and unprecedented photostability.

1. Introduction

Hydrogen production from direct splitting of water using semiconductor photocatalysts is regarded as a promising way to produce clean energy and remedy environment problems [1]. Among all reported semiconductor photocatalysts, CdS possesses a suitable band gap ($E_g = 2.4$ eV) for visible light absorption and sufficiently negative conduction band potential for proton reduction, making it a most popular photocatalyst for visible-light-driven photocatalytic hydrogen production from water splitting [2–5]. It is well known that the photocatalytic activity of bare CdS crystals is mainly determined by the morphological, crystalline structure, specific surface area, and crystalline size [6,7]. Up to now, various methods have been carried out for modifications of pure CdS photocatalyst, such as hollow nanorods [8], flowers [9], nanowires [7,10], nanospheres [11] and nanocubes [12]. Unfortunately, the disadvantages of pristine CdS are mainly limited by rapid photoexciton recombination and the photocorrosion [13–18].

Therefore, it is a constantly challenging issue to develop highly active CdS photocatalysts with good photocorrosion resistance for hydrogen evolution.

Recently, the facet-engineered surface design for semiconductor has been proven as a versatile approach to enhance their photocatalytic performance, due to the fascinating shape-dependent photocatalytic activity [19,20]. For instance, the exposed facet {001} in WO₃, {110} in BiOCl, {112} in Co₃O₄, {001} in PbTiO₃ and {111} in AgIn₃S₈ were proved to be more efficient than other facets in photocatalytic water oxidation or reduction [21–25]. Recent works on crystal facet engineering of semiconductors have demonstrated that photoexcited electrons and holes may be driven to different crystal facets, which can realize the effective spatial separation of photogenerated electrons and holes [26–31]. The effective spatial separation of photogenerated electrons and holes is critical to improvement of the photocatalytic performance [13,32]. It is reported that photogenerated electrons and holes tend to migrate to {010} and {110} exposed facets of BiVO₄,

* Corresponding author at: School of Chemistry and Chemical Engineering, Nanjing University, Nanjing, 210023, PR China.
E-mail address: wangy@nju.edu.cn (Y. Wang).

respectively, which greatly enhanced its photocatalytic oxygen evolution activity [26]. In addition, with the co-exposed {023} and {001} in SrTiO_3 , {001} and {110} in $\text{Bi}_3\text{TiNbO}_9$, {001} and {101} in TiO_2 realized effective charge separation between different crystal facets that significantly enhanced the photocatalytic water splitting and CO_2 reduction activity [27–30]. Most recently, the “surface heterojunction” or “facet junction” concept is proposed to further explain the difference in the photocatalytic activity of TiO_2 single crystals with co-exposed {001} and {101} facets [31,33]. Such a self-constructed {001}/{101} facet junction in TiO_2 single crystals with continuous band bending by type-II band alignment significantly promoted the separation rate of photo-generated electrons and holes [33]. As for extensively studied CdS photocatalyst, previous investigations demonstrated that the hexagonal CdS exhibits a higher photocatalytic activity than cubic CdS and the hexagonal CdS crystal with the largest {0001} facets are usually found to be more reactive for photocatalytic hydrogen evolution because of its higher surface energy [3,34,35]. However, the photocatalytic hydrogen evolution activity of these crystal facet-engineered CdS with {0001} facets are unsatisfactory and even there is no report to date that a self-constructed facet junction between {0001} and {1010} on hexagonal CdS single crystals for highly efficient photocatalytic hydrogen evolution with unprecedented photostability.

In this work, a novel facet-junction engineered monodispersed hexagonal CdS single crystals with layered stacking hexagonal shape nanoplates were synthesized by hydrothermal reaction via adjusting the molar ratio of S/Cd precursor. Na_2S might serve as the structure-directing agents for the hexagonal CdS growth. As the S/Cd molar ratio increasing, the crystalline phase structure of CdS gradually transform from a mixed cubic/hexagonal phase structure into pure hexagonal phase with different exposed facets. The co-exposed {0001} and {1010} facets on hexagonal CdS single crystals with well-defined epitaxial interfaces showed highly efficient visible-light-induced H_2 evolution. The type-II band alignment between co-exposed {0001} and {1010} facets constructing facet junction with continuous band bending that significantly promoted the separation rate of photo-generated electrons and holes. Such a facet-mediated charge separation on hexagonal CdS single crystals by self-constructed {0001}/{1010} facet junction is proved by self-selective photo-deposition of Pt nanoparticles on the exposed {0001} facets which serve as the active surfaces for photocatalytic hydrogen production. In addition, the small amount of sulfur vacancies are also benefit for the hydrogen evolution activity of CdS-5, which can largely reduce the bulk electron-hole recombination. The time-resolved fluorescence (TRPL) decay and photoelectrochemical test further proved the effective spatial charge separation. As a consequence, a high stable and excellent photocatalytic activity are obtained over facet-junction engineered hexagonal CdS single crystals. This work provides a feasible and simple strategy for designing of facet-junction engineered CdS single crystals with highly efficient photocatalytic activity and unprecedented photostability.

2. Experimental section

2.1. Preparation of photocatalysts

CdS photocatalysts with different molar ratio of Cd/S were prepared by a one-step hydrothermal method. Typically, 10 mmol Cd (NO_3)₂·4H₂O and Na₂S·9H₂O was dissolved in 25 mL deionized water to form a orange slurry under magnetic stirring condition at room temperature. After stirring for 60 min, the orange slurry precursor solution was then transferred into a 50 mL Teflon-lined autoclave and maintained at 200 °C for 20 h. Finally, the precipitate was obtained by centrifugation and washed several times with deionized water and ethanol and vacuum dried at 60 °C overnight. The molar ratio of Cd (NO_3)₂·4H₂O to Na₂S·9H₂O was fixed as 1:1, 1:2, 1:3, 1:4, 1:5, 1:6 and 1:7 (namely, molar ratio Cd/S = 1:1, 1:2, 1:3, 1:4, 1:5, 1:6 and 1:7) and obtained products were named as CdS-X, that is, CdS-1, CdS-2, CdS-3,

CdS-4, CdS-5, CdS-6 and CdS-7 respectively.

2.2. Characterizations

Powder X-ray diffraction (PXRD) data were collected using a Rigaku Ultima III X-ray diffractometer using Cu K α radiation ($\lambda = 1.54056 \text{ \AA}$). Scanning electron microscope (SEM) images were recorded with a Hitachi S4800 FE-SEM system. Transmission electron microscope (TEM) and high-resolution transmission electron microscope (HRTEM) images were obtained by using a JEM-2100 electron microscope. Chemical states of the CdS samples were characterized by a PHI 5000 Versa Probe X-ray photoelectron spectrometer (a monochromatic Al Ka X-ray radiation). All of the binding energies of all elements were calibrated by the C 1 s peak at 284.6 eV. UV – vis spectra were collected using a Shimadzu UV-3600 spectrometer, BaSO₄ was used as reference. The photoluminescence (PL) spectra were taken on a Horiba Scientific FluoroMax-4 fluorometer spectrometer at room temperature and time-resolved fluorescence emission spectrum were conducted with Horiba Jobin Yvon Data Station by time-correlated single-photon counting. The surface photovoltage spectra (SPV) were performed on a home-built apparatus, which consists of a 500 W Xe lamp (CHF XM500 W, Beijing Trusttech Co. Ltd., China), a double-grating monochromator (Zolix SP500), a lock-in amplifier (SR830-DSP) and a light chopper (SR540). The construction of the photovoltaic cell is of a sandwich structure.

2.3. Photocatalytic hydrogen evolution

The photocatalytic hydrogen evolution reactions were conducted in a side-irradiation Pyrex reactor, which connected to a glass-closed gas circulation system at ambient temperature. In a typical photocatalytic experiment, 30 mg of catalyst power was suspended in 400 mL aqueous solution containing 0.35 M Na_2S and 0.25 M Na_2SO_3 as the sacrificial agent of the hole. Before visible light irradiation, the reactant system was degassed by evacuation under low temperature condition (liquid nitrogen) to remove air and ensure that the reaction system was under anaerobic conditions, and then was irradiated by a 300-W Xe lamp with a cutoff filter of 420 nm for H_2 evolution under magnetic stirring condition. The amount of hydrogen evolution was analyzed by an online gas chromatograph (GC-14C, Shimadzu, TCD, Ar as carrier).

In the apparent quantum efficiency (AQE) test, the reaction mixtures were irradiated for 1 h. AQE was calculated using the following equation:

$$\text{AQE} = \frac{2 \times \text{the number of evolved hydrogen molecules}}{\text{the number of incident photons}} \times 100\%$$

2.4. Electrochemical measurements

The photoelectrochemical measurement was performed on an electrochemical analyzer (Chenhua CHI 660D) in a standard three-electrode cell. The working electrodes were prepared as follows: 5 mg of photocatalyst powder and 20 μL 0.25% Nafion were dispersed into 1.0 mL ethanol, and then ultrasonic treatment for 1 h. 40 μL of dispersion solution was then directly coated onto the pre-cleaned indium tin oxide glass (ITO glass) surface ($1 \times 2 \text{ cm}^2$). Finally, the obtained electrodes were heated to 100 °C for 1 h in the oven. Platinum wire was used as the counter electrode, and a saturated calomel electrode (SCE) was used as the reference electrode. $E^\circ = 0.241 \text{ V vs. NHE}$ at 25 °C for saturated calomel electrode. The Mott-Schottky curves were taken under dark with a voltage of 5 mV at a frequency of 1 kHz. The potential ranged from -1.3 to 1.7 V (vs. SCE). Electrochemical impedance spectroscopy (EIS) plots were collected at opencircuit potential (0.5 V vs. SCE), with the frequency ranging from 100 kHz to 0.01 Hz and the modulation amplitude of 5 mV. The transient photocurrent measurements were recorded at an applied potential of 0.5 V vs. SCE under the visible illumination. A 300-W Xe lamp equipped with an optical

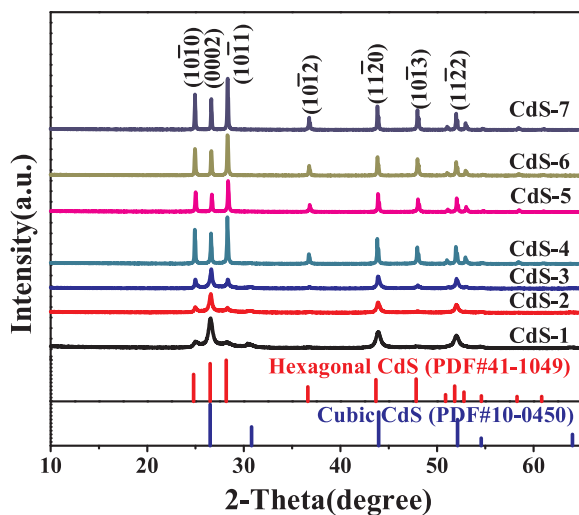


Fig. 1. XRD patterns of Cds-1, Cds-2, Cds-3, Cds-4, Cds-5, Cds-6 and Cds-7 samples.

cutoff filter of 420 nm was employed for the visible-light excitation. The electrocatalytic activity of the samples were examined by obtaining polarization curves using linear sweep voltammetry (LSV) with a scan rate of 5 mV s^{-1} at room temperature.

3. Results and discussion

A series of CdS samples were successfully synthesized through a one-step hydrothermal method at 200°C with different molar ratio of S/Cd precursor. The crystal structure and phase purity of the as-prepared CdS samples were examined by powder X-ray diffraction (XRD). As shown in Fig. 1, the hexagonal phase content is established gradually along with the increase in S/Cd precursor molar ratio, and then the hexagonal phase becomes predominant and gradually transforms into pure hexagonal phase, indicating the crystalline phase structures are governed by the molar ratio of S/Cd precursor in the hydrothermal reaction. In Figs. 1 and S1, Cds-1, Cds-2, Cds-3 and Cds-4 show a mixed cubic/hexagonal phase, while all the diffraction peaks of the Cds-5, Cds-6 and Cds-7 can be indexed as the pure hexagonal CdS (JCPDS#41-1049) with lattice constants $a = 4.139 \text{ \AA}$ and $c = 6.720 \text{ \AA}$ [10,14]. It is concluded that the Na₂S might serve as the structure-directing agents for the hexagonal CdS growth. No peaks of impurities were detected, indicating the high purity of the product. Notably, the stronger and sharper diffraction peaks in the pattern of these samples suggest a gradually enhanced crystallinity as the molar ratio of S/Cd increase.

The effect of S/Cd molar ratio precursor on morphology and structure of these as-prepared CdS samples were investigated in detail by SEM, as illustrated in Fig. 2. The shape and size of the CdS are very sensitive to the molar ratio of S/Cd precursor. The Cds-1 powder shows a spherical-like structure (Fig. 2a). As S/Cd molar ratio increasing from 1:1 to 3:1 (Fig. 2a-c), the pyramidal CdS gradually appears with the size significantly increased, which is characteristic of Ostwald-ripening mechanism of crystal growth. When the S/Cd molar ratio is up to 4:1, most of CdS particles grow into polyhedron shape with big size (Fig. 2d). And continue to increase S/Cd molar ratio, it can be clearly observed that the Cds-5, Cds-6 and Cds-7 grown into big pyramidal polyhedron hexagonal single crystals with few layered stacking hexagonal shape nanoplates on the top, possessing a smooth surface, as well as well separated from each other. (Fig. 2e-g). Interestingly, the pyramidal polyhedron CdS single crystals presented some smaller crystals adherent to larger ones. Meanwhile, the crystal phase of CdS gradually transforms into pure hexagonal phase (Cds-5, Cds-6 and Cds-7) from a mixed cubic-hexagonal phase (Cds-1, Cds-2, Cds-3 and Cds-4).

4) with the S/Cd molar ratio increasing. This proves that the Na₂S plays a crucial role to control the final morphology and crystal phase of the product. The model image insert in Fig. 2e is the representative hexagonal polyhedron CdS single crystals under sulfur-rich environment. These result indicated the hexagonal crystal structure of CdS dominated the growth of the polyhedron crystallites under sulfur-rich growth environment. Also, the growth of hexagonal CdS single crystal in sulfur-rich environment was attributed to the highly anisotropic crystal structure and the structure-directing effect of Na₂S. Notably, as the sulfur precursor increased, more exposed facets were observed with hexagonal crystal structure formation. The relative stability of each facet during crystal growth is intrinsically determined by the surface energies of the facet [20]. It also revealed that the Na₂S is very effective in changing the surface energy of CdS and thus change the morphological by increasing the S/Cd molar ratio. It is expected that these more exposed facets in hexagonal CdS single crystal have significant effect on the charge carrier separation and transfer during photocatalytic hydrogen evolution process.

The morphology and structure of Cds-1 and Cds-5 were further analyzed by TEM. As shows in Fig. 3a, the Cds-1 exhibits irregular nanoparticles with partial pyramidal shape and the size distribution of $20 \sim 50 \text{ nm}$. Combining the SEM results (Fig. 2), it can be conclude that the pyramidal polyhedral shape structure of CdS is governed by the molar ratio of S/Cd precursor in the hydrothermal reaction and the Cds-1, Cds-2, Cds-3 and Cds-4 are not have enough Na₂S to completely transform into hexagonal polyhedral CdS single crystals [36]. In Fig. 3b, a representative hexagonal shape nanoplate on the top view of Cds-5 was clearly observed from [0001] direction. And a highly ordered continuous crystal lattice fringe pattern with the spacing of 0.336 nm is clearly observed in the insert image (Fig. 3b), matched well with the {0001} plane of hexagonal CdS. The selected area electron diffraction (SAED) pattern of hexagonal polyhedral Cds-5 indicates the single-crystal nature. Fig. 3c shows the tip surface of hexagonal polyhedral Cds-5 single crystal is a flat surface and the lateral surfaces presented a stepped surface. And the lattice fringes spacing is 0.356 nm in HRTEM image (Fig. 3c), corresponding to the {1010} plane of hexagonal CdS. This structure is like the top surface of Cds-5 single crystal with layered stacking hexagonal shape nanoplates. These nanoplates are appeared to be merged with each other forming the stepped surfaces. Thus, the flat surface is {0001} facet, while the lateral surface is a vertical {1010} facet. In Fig. 3d, the red circle region is a sloping side surface with lattice fringes spacing is 0.319 nm , which is corresponding to the {1011} plane. More clearly, the schematic diagram for hexagonal polyhedral Cds-5 single crystal with {0001}, {1010} and {1011} facets is presented in the Fig. 3e. Notably, the hexagonal polyhedral CdS single crystal is mainly composed by layered stacking hexagonal shape nanoplates which only have {0001} and {1010} facets. As expected, the exposed facets formation of {0001}/{1010} facet junctions in hexagonal nanoplates for efficient charge carriers separation and transfer.

To better understand the formation mechanism of hexagonal polyhedral CdS single crystal with layered stacking hexagonal shape nanoplates structure, Cds-5 was selected as a representative for further study in detail by SEM. In Fig. S2a and Fig. S3a-b, Cds-5 prepared at room temperature (Cds-5-RT) shows spherical-like particles with serious agglomeration. This phenomenon is because of the small solubility K_{sp} (8.0×10^{-27}) of CdS, Cd²⁺ rapidly reacts with S²⁻, which results in a fast nucleation of fine CdS nanocrystals that suffer from disadvantages of particles agglomeration [8,35]. The TEM images (Fig. S3c-d) further proved the spherical-like charters of Cds-5-RT particles, and the size is around 10 nm . Moreover, the Cds-5-RT is a pure cubic phase CdS (JCPDS#10-0454) (Fig. S4a) [2]. Fig. S2b-f shows the change of morphology and size for the produced Cds-5 with the hydrothermal time increasing to different time at 200°C . After the first hour of hydrothermal reaction, the Cds-5-1 h undergo self-assembly and form small nanoparticles and the size slight bigger than Cds-5-RT. And a small of crystal phase transformed into hexagonal phase structure, a mixed

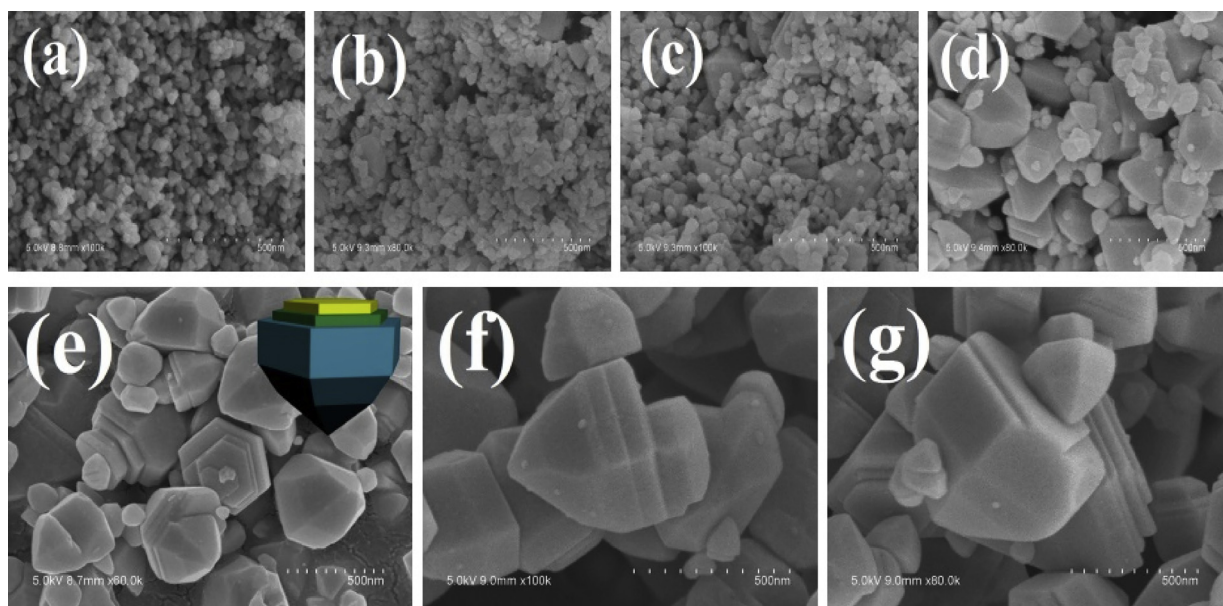


Fig. 2. SEM images of (a) CdS-1, (b) CdS-2, (c) CdS-3, (d) CdS-4, (e) CdS-5, (f) CdS-6 and (g) CdS-7.

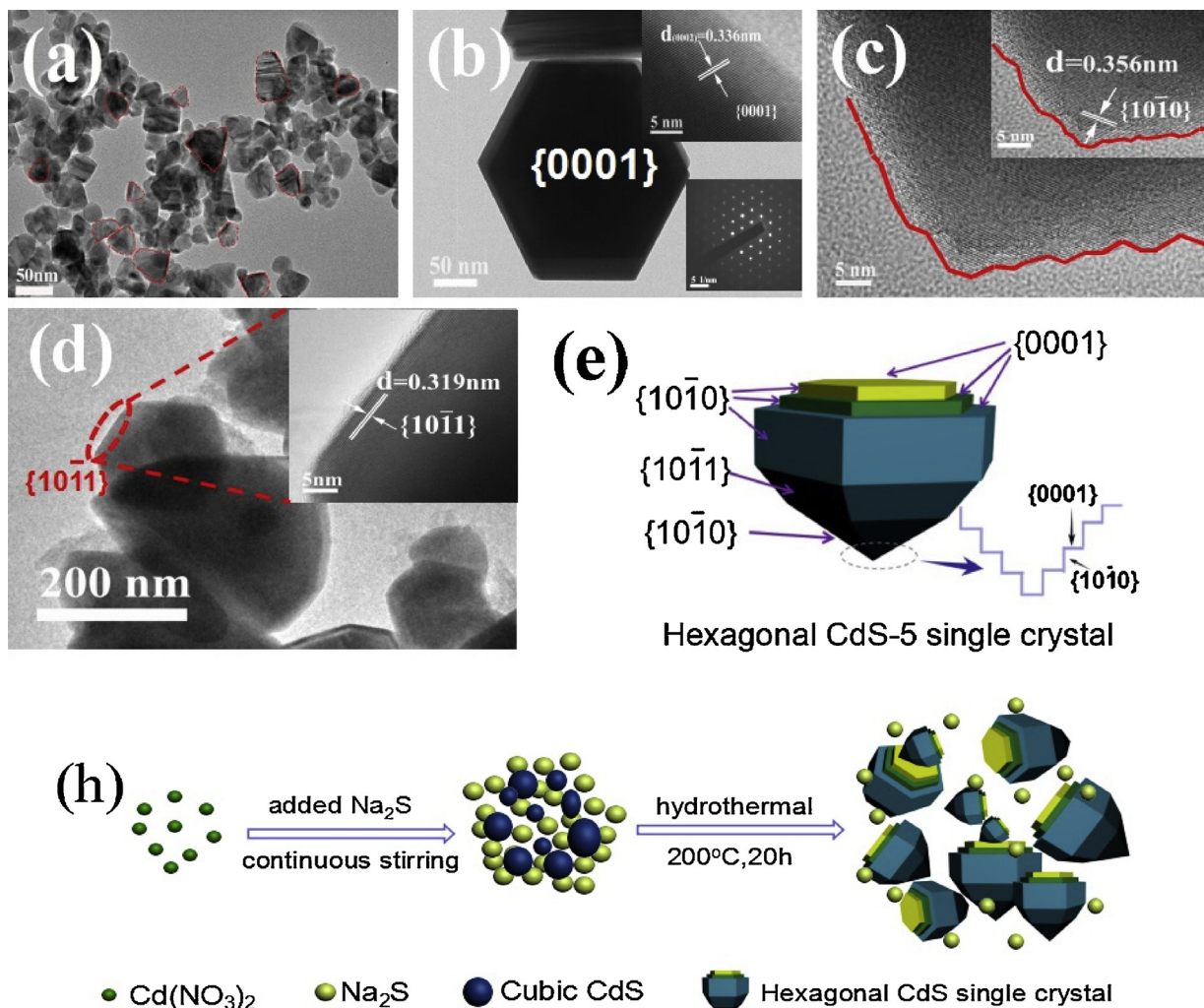


Fig. 3. TEM images of (a) CdS-1 and (b-d) CdS-5 samples; (e) Schematic diagram for hexagonal CdS-5 single crystal with $\{0001\}$, $\{10\bar{1}0\}$ and $\{10\bar{1}1\}$ facets. (h) Scheme of hydrothermal growth for hexagonal polyhedral CdS single crystal.

cubic-hexagonal phase of CdS-5-1 h was clearly observed in the XRD results (Fig. S4). CdS-5-5 h displays a small size particles coated hexagonal polyhedral CdS single crystals after 5 h hydrothermal reaction, and the layered stacking hexagonal shape nanoplates also shown in polyhedral CdS single crystals. More clearly, it can be observed more different sizes of layered stacking hexagonal shape nanoplates in CdS-5-10 h with more exposed {0001} and {1010} facets, which composition of the hexagonal polyhedral CdS single crystal structure. With the hydrothermal time increasing, the layered stacking hexagonal shape nanoplates are still existence in CdS-5 (15 h and 20 h) single crystal structure and the crystal growth is more perfect (Figs. S2e-f and S4). According to about results, it can be concluded that the hexagonal polyhedral CdS single crystal was composed by different sizes of layered stacking hexagonal shape nanoplates. Because of the higher surface energy of {0001} facet than that of the other faces, leading to {0001} facets grow fast and exhibit small facets at the beginning [34,35]. It is reported that the {0001} facets possess 100% Cd_{3c} atoms, on the contrary, {1010} facets possess 50% Cd_{3c} and 50% saturated four-coordinate Cd atoms (Cd_{4c}) [35]. The {0001} facets with 100% Cd_{3c} atoms produced positively charged and covered by the adsorbing S²⁻ through electrostatic interaction in sulfur-rich environment, resulting in terminate growth along the [0001] surface. As a result, the hexagonal shape nanoplates with {0001} facets formed. Because of the different diffusion concentration of Cd²⁺ to the formed {0001} surfaces from the uneven size of small CdS particles in the Ostwald-ripening process of crystal growth, the different sizes of hexagonal shape nanoplates formed and self-assembly into layered stacking hexagonal shape nanoplates structure of hexagonal polyhedral CdS single crystal.

The surface chemical compositions of CdS were confirmed by the X-ray photoelectron spectroscopy (XPS). As depicted in Fig. 4a, the binding energies of Cd 3d for CdS-5 at 404.68 and 411.45 eV, corresponding to the Cd 3d_{5/2} and Cd 3d_{3/2}, which slightly shifted about 0.02 ~ 0.03 eV towards low binding energies relative to CdS-1. The S 2p XPS spectrum for CdS-5 (Fig. 4b) shows two peaks at 161.15 and 162.43 eV can be attributed to the S 2p_{3/2} and S 2p_{1/2} for the S²⁻, respectively. While the S 2p XPS spectrum for CdS-1 exhibits lower binding energies, which centered at 161.12 eV (S 2p_{3/2}) and 162.31 eV (S 2p_{1/2}). The XPS quantitative analysis results of Cd:S atomic ratio for CdS-1 and CdS-5 are listed in Table S1 in detail. The Cd:S atomic ratio of CdS-1 and CdS-5 are 1:0.77 and 1:1.03, respectively, indicating that the S vacancies exist in CdS-1. The existence of S vacancies may be accounting for the shifted binding energies, which results in the change of electronic density around the Cd and S atoms [37,38].

The optical properties of CdS-1, CdS-2, CdS-3, CdS-4, CdS-5, CdS-6 and CdS-7 samples are investigated by the UV-vis diffuse reflectance spectra (UV-vis DRS). As shown in Fig. 5a, it can be seen that CdS-1 has a strong visible absorption edges of 540 nm, and all of photoabsorption

edges of these samples gradually blue-shifted from 540 nm to 516 nm for CdS-1 to CdS-7. This maybe caused by the particles size and crystallinity of CdS, which leading to the color change of samples from orange (CdS-1) to bright yellow (CdS-7) that can be seen in the inset of Fig. 5a. The corresponding band gap energies can be calculated by the Tauc equation: $a\hbar v = A(h\nu - E_g)^{1/2}$ for the direct band gap material, based on the tangent lines of $(a\hbar v)^2$ to $\hbar v$ plots (where a is the absorption coefficient and $\hbar v$ is the photon energy) [38]. As displayed in Fig. 5b, the band gap is gradually widening from CdS-1 to CdS-7. In Fig. S5, the bandgap of CdS-1, CdS-2, CdS-3, CdS-4, CdS-5, CdS-6 and CdS-7 samples are 2.339, 2.341, 2.358, 2.413, 2.417, 2.421 and 2.422 eV, respectively.

Mott – Schottky curves are employed to evaluate the flat-band potential (E_{fb}) of CdS photocatalysts in 0.5 M Na₂SO₄ electrolyte at three different frequencies. As presented in Fig. S6, the positive slopes of C⁻²–E plots indicate that CdS is an n-type semiconductor. The E_{fb} of CdS-1, CdS-2, CdS-3, CdS-4, CdS-5, CdS-6 and CdS-7 are –0.28, –0.39, –0.43, –0.60, –0.73, –0.83 and –0.84 V versus SCE, respectively. It is known that the conduction band potential (E_{CB}) is generally more negative about –0.1 or –0.2 V than its flat band potential for n-type semiconductor [39]. And thus, the E_{CB} for CdS-1, CdS-2, CdS-3, CdS-4, CdS-5, CdS-6 and CdS-7 are roughly reckon up to be –0.24, –0.35, –0.39, –0.56, –0.69, –0.79 and –0.80 V vs. normal hydrogen electrode (NHE) ($E_{NHE} = E_{SCE} + 0.241$ V), respectively. The gradually negative conduction band thermodynamically indicates that the proton reduction ability gradually increases for H₂ production. Furthermore, considering the band gap and above results, the valence band (E_{VB}) are 2.099, 1.991, 1.968, 1.853, 1.727, 1.631 and 1.622 V for CdS-1, CdS-2, CdS-3, CdS-4, CdS-5, CdS-6 and CdS-7, respectively. The decreased E_{VB} indicates the weakened oxidation capacity for photocorrosion. More clearly, the band structure diagram of the seven kinds of CdS samples are schematically illustrated in Fig. S7.

Furthermore, the photoluminescence (PL) spectra are measured to further evaluate the modulation effect of Na₂S content on CdS sample in hydrothermal process. Fig. 5c shows the typical PL spectra of CdS sample excited at 380 nm. An emission band around 563 nm is observed from CdS-1, which is usually attributed to the shallow trap caused by surface states such as sulfur vacancies or sulfur dangling bonds [6,40]. The XPS quantitative analysis results of S/Cd atomic ratio further confirmed the PL emission is related to the sulfur vacancy, which is generally attributed to the recombination of trapped electrons in sulfur vacancy with holes in the valence band [14]. It can be clearly observed that the intensity of PL emission gradually increased from CdS-1 to CdS-7 samples. This is due to the reduction of sulfur vacancies at grain boundaries with the crystallinity of CdS increased. The sulfur vacancies are carrier trappers, where photogenerated electrons and holes are trapped [14]. As a result, the irradiative recombination of photoexcited

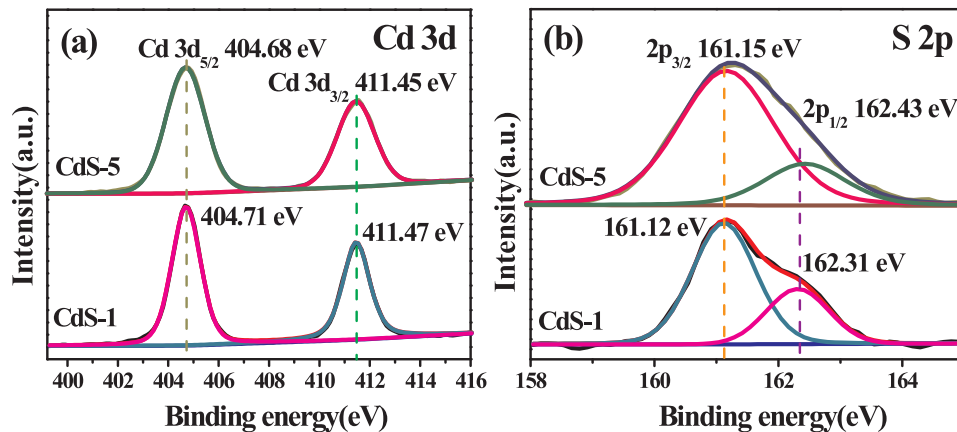


Fig. 4. XPS spectra of (a) Cd 3d and (b) S 2p for the CdS-1 and CdS-5 samples.

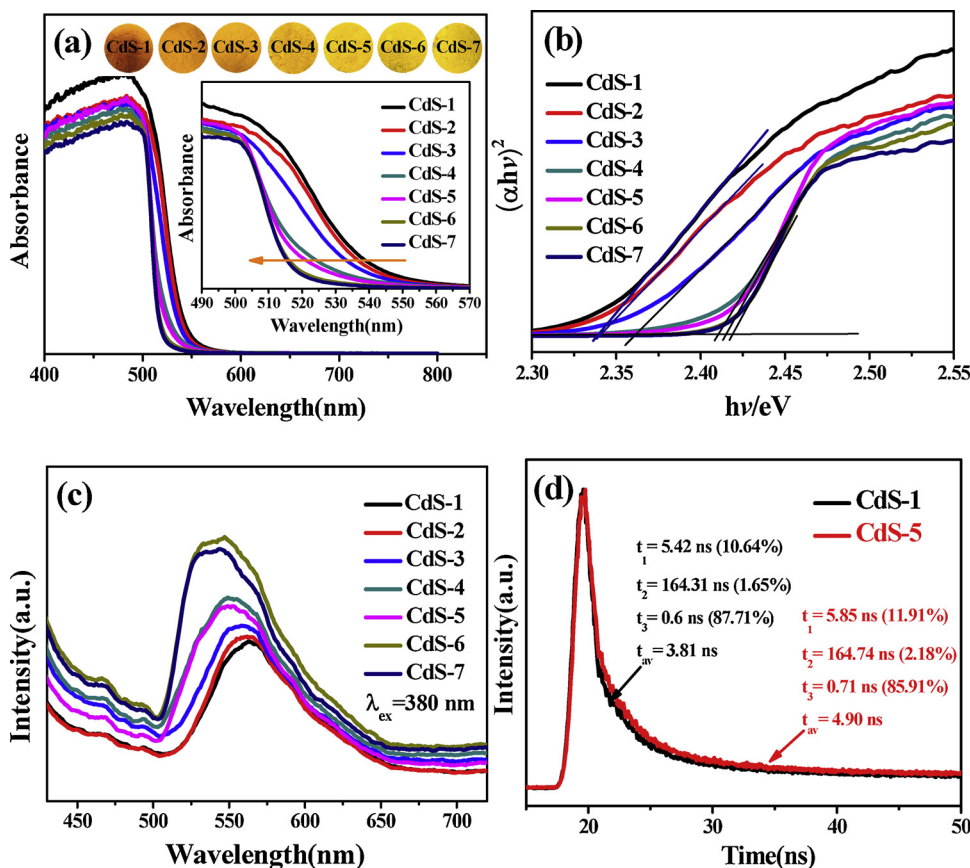


Fig. 5. (a) UV-vis diffuse reflectance spectra of CdS-1, CdS-2, CdS-3, CdS-4, CdS-5, CdS-6 and CdS-7 samples and (b) the corresponding $(\alpha h\nu)^2$ vs photon energy curves; (c) PL spectra of CdS-1, CdS-2, CdS-3, CdS-4, CdS-5, CdS-6 and CdS-7 samples excited at 380 nm; (d) Time-resolved fluorescence spectra (TRPL) of CdS-1 and CdS-5.

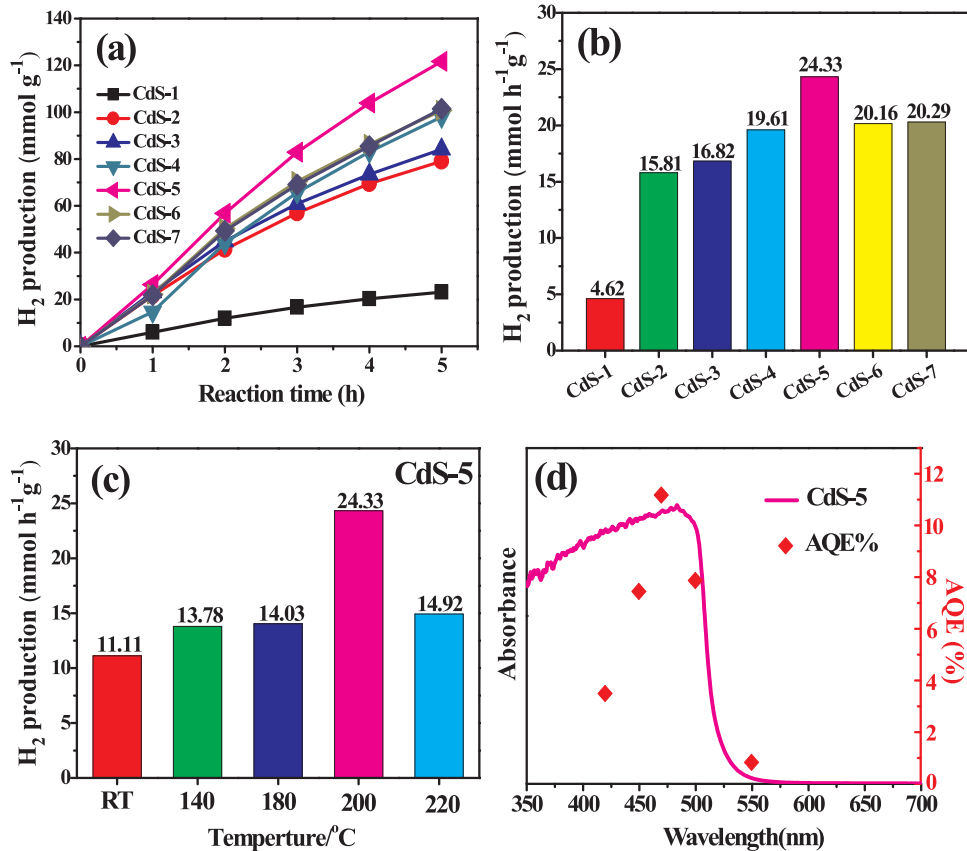


Fig. 6. (a) Time dependent photocatalytic H₂ evolution and (b) average hydrogen production rates of CdS-1, CdS-2, CdS-3, CdS-4, CdS-5, CdS-6 and CdS-7 under visible light irradiation ($\lambda \geq 420$ nm); (c) corresponding relationship between the hydrothermal temperature and photocatalytic H₂ production rates for CdS-5; (d) the wavelength dependent AQE of hydrogen evolution over CdS-5 sample.

carriers is enhanced leading to intensive PL emission. The more intensive PL emission is the exact proof of reduced sulfur vacancies resulting from more Na₂S used in hydrothermal process, which is well matched with the enhanced crystallinity of CdS. Additionally, the gradually blue-shifted PL emission from CdS-1 to CdS-7 indicates the Stoke's shifts are largely reduced, further confirming that the sulfur vacancies of CdS are effectively passivated [2]. Furthermore, the energy level of sulfur vacancies on CdS-1 and CdS-5 are detected by the Stoke's shifts. The CdS-6 and CdS-7 are considered as perfect crystal without defect because of the PL emissions of CdS-6 and CdS-7 are identical. So taking the emission of CdS-7 as a standard, photon energies of CdS-1 and CdS-5 to CdS-7 are calculated. As shown in Fig. S8a, the PL energy of CdS-1, CdS-5 and CdS-7 are 2.20, 2.25 and 2.30 eV, respectively, according to the formula: $E = 1240/\lambda$ (λ is the PL emission). The photon energy differences (ΔE) of CdS-1 and CdS-5 to CdS-7 are $\Delta E_1 = 0.10$ eV and $\Delta E_2 = 0.05$ eV, respectively. In this work, the red shifts of CdS-1 and CdS-5 are resulting from the sulfur vacancies compared to CdS-7, thus the differences of photon energy indicate the energy level of sulfur vacancies (Vs) according to the principles of fluorescence spectroscopy. Due to the sulfur vacancy is a shallow trap state, so the energy level of sulfur vacancies of CdS-1 and CdS-5 are 0.10 and 0.05 eV below the conduction band (CB), respectively. More clearly, the corresponding scheme for the energy level of CdS-1, CdS-5 and CdS-7 are schematically illustrated in Fig. S8b.

Moreover, the time-resolved PL spectra are performed to explore the charge transfer dynamic events of CdS-1 and CdS-5. By the three-exponential fitting, the average PL lifetime $\langle \tau_{av} \rangle$ of CdS-1 and CdS-5 are calculated and presented in Fig. 5d. The average PL lifetime increased from 3.81 ns (CdS-1) to 4.90 ns (CdS-5) with increasing of Na₂S used. The elongating average PL lifetime indicates that the separation efficiency of photogenerated charge carriers is increased, which is beneficial for the photocatalytic hydrogen evolution [41].

The photocatalytic H₂ evolution activity of the samples were performed using 0.35 M Na₂S and 0.25 M Na₂SO₃ aqueous solution as hole sacrificial agent under visible-light irradiation ($\lambda \geq 420$ nm), as presented in Fig. 6. The CdS-1 shows the lowest photocatalytic H₂ evolution activity of 23.11 mmol g⁻¹ over 5 h, whereas the CdS-5 exhibits the highest photocatalytic activity of 121.66 mmol g⁻¹ in all of samples, the 5.3 times enhancement in photoactivity indicates that the high efficient charge separation and transfer of CdS-5 for improving the surface hydrogen evolution kinetics. The {0001} facet is crucial role for improving the photocatalytic H₂ evolution activity under visible light irradiation. As displayed in Fig. S9, the SEM image shows that Pt particles were self-selectively photodeposited onto the {0001} facets of CdS-5 in presence of hole sacrificial agent under visible-light irradiation, indicating the {0001} is the active facet for photocatalytic hydrogen production because it is the electron-collecting facet. In Fig. 6a, the photocatalytic activity of the Na₂S engineered CdS is increased with the S/Cd molar ratio increasing, indicating the {0001} active facet is increased. Fig. 6b shows that all of the CdS samples exhibit an enhanced photocatalytic H₂ production rate compared to CdS-1, and the hydrogen evolution rate increased with the increasing S/Cd molar ratio. The corresponding H₂ production rates are 4.62 mmol h⁻¹ g⁻¹, 15.81 mmol h⁻¹ g⁻¹, 16.82 mmol h⁻¹ g⁻¹, 19.61 mmol h⁻¹ g⁻¹, 24.33 mmol h⁻¹ g⁻¹, 20.16 mmol h⁻¹ g⁻¹ and 20.29 mmol h⁻¹ g⁻¹ for the CdS-1, CdS-2, CdS-3, CdS-4, CdS-5, CdS-6, and CdS-7 samples, respectively. The significantly higher photoactivity of the CdS-5 should be ascribed to the presence of the self-constructed {0001}/{10̄0} facet junction and the highly mono-dispersed single crystals in sacrificial agent aqueous solution, which accelerated carrier separation and transfer. Previous work about density of state (DOS) for CdS has shown that both the CB and VB positions of {10̄0} facets are more negative than {0001}[35]. The type-II band alignment between {0001} and {10̄0} facets is well-known for charge separation [33,35]. Specifically, photogenerated electrons transfer to {0001} facets for reduction while photogenerated holes accumulate on {10̄0} facets for oxidation [35].

An excessive surface exposure of the {0001} or {10̄0} facet on the facet-junction engineered CdS might cause a hole or electron overflow effect to restrict photochemical reactions [33]. In addition, compared with CdS-1 to CdS-4, CdS-5 has well hexagonal shape and less sulfur vacancies, as well as the highest photoactivity. This indicates the self-constructed facet junction dominant the photocatalytic activity. Moreover, CdS-6 and CdS-7 have similar hexagonal shape with CdS-5 and more less sulfur vacancies but the photocatalytic activities is lower than CdS-5. Thus, the sulfur vacancies are also benefit for the hydrogen evolution activity of CdS-5. The best photocatalytic hydrogen evolution activity of CdS-5 can be attributed to the synergistic effect of self-constructed facet junction and sulfur vacancies. Fig. 6c investigates the hydrothermal temperature dependence of photocatalytic H₂ evolution activity and the CdS-5 with synthesis temperature of 200 °C shows the highest photocatalytic activity. A comparison with previous similar works about CdS photocatalyst for photocatalytic H₂ production activity is listed in Table S2. It can be clearly seen from the table that the present approach leads to outstanding photocatalytic H₂ production activity without any co-catalyst compared to other works. This can be further demonstrated the advantages of the self-constructed {0001}/{10̄0} facet junction of CdS single crystals for photocatalysis. Additionally, the wavelength dependent apparent quantum efficiency (AQE) of hydrogen evolution is given in Fig. 6d, a highest AQE of 11.18% is obtained at 470 nm for facet-junction engineered hexagonal CdS-5 single crystals that are consistent with the light absorption capacity.

More importantly, the facet-junction-engineered hexagonal CdS-5 shows very high photocatalytic stability for hydrogen production in comparison with CdS-1 under visible-light irradiation ($\lambda \geq 420$ nm). As shown in Fig. 7, the photoactivity of CdS-1 is significantly decreased after 4 consecutive cycles (16 h) under visible light irradiation due to the strong photocorrosion, and only keeps 15.3% photoactivity. Compared with the CdS-1, CdS-5 shows superior photostability for H₂ evolution, even after 25 consecutive cycles during 100 h light irradiation that impregnated in the strong alkaline sacrificial agent beyond 20 days, the initial photoactivity is still remained. This long-term photostability of CdS-5 for H₂ evolution can be attributed to the self-constructed {0001}/{10̄0} facet junction, which remarkably improved the separation efficiency of photogenerated electrons and holes on the surface of CdS-5. The unique morphological and structural stabilities of the used CdS-5 were further confirmed by the characterization results in Fig. S10 and Fig. S11. In Fig. S10, the SEM images of used CdS-1 nanoparticles indicate that severe agglomeration occurred due to the photocorrosion in comparison with fresh sample. And the used CdS-5 is still remained the well crystal structure with a smooth surface after 100 h light irradiation that impregnated in the strong alkaline sacrificial

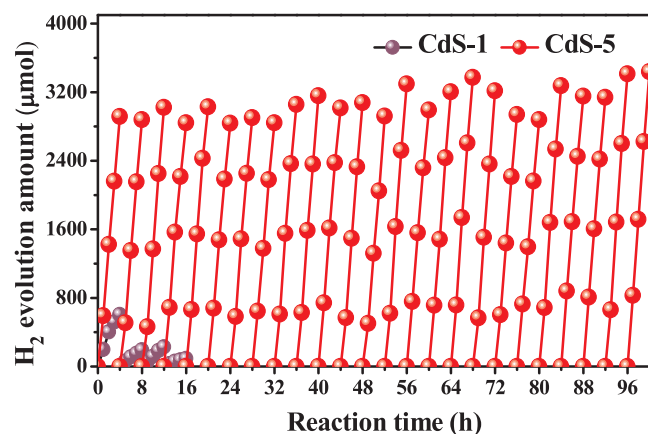


Fig. 7. Photostability for the H₂ production of CdS-1 and CdS-5 under visible light irradiation ($\lambda \geq 420$ nm). Reaction condition: 30 mg catalyst dispersed in 400 mL 0.35 M Na₂S and 0.25 M Na₂SO₃ sacrificial reagent aqueous solution.

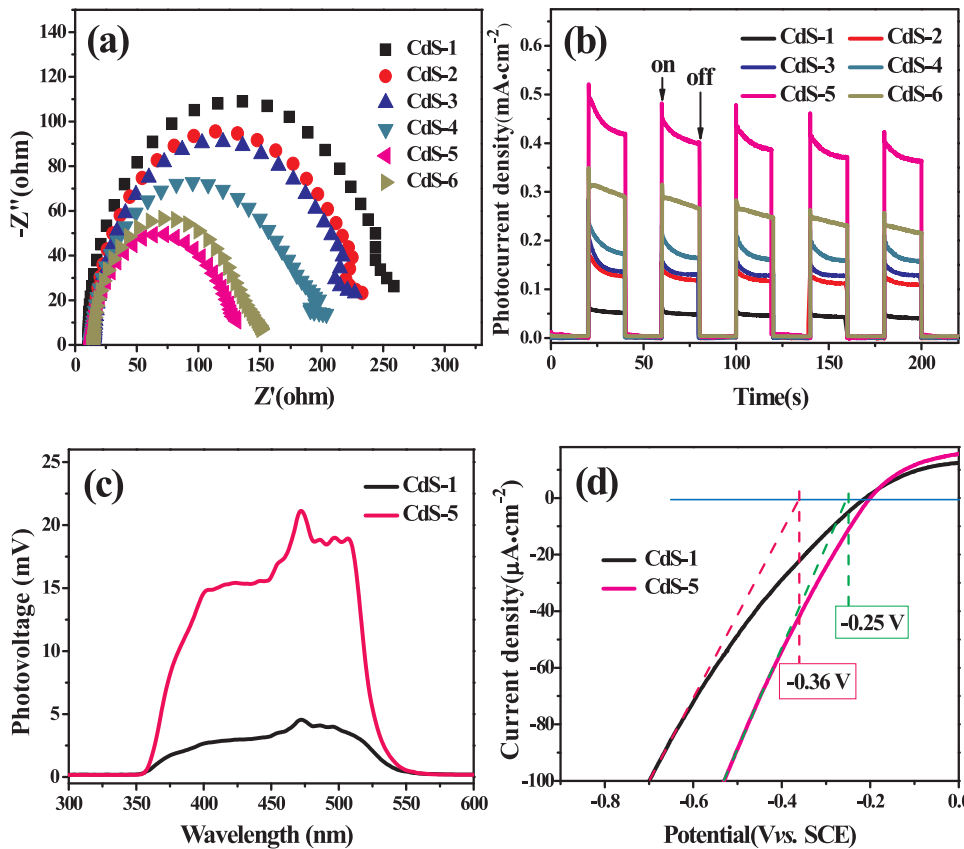


Fig. 8. (a) Nyquist plots of electrochemical impedance spectroscopy (EIS) for CdS-1, CdS-2, CdS-3, CdS-4, CdS-5 and CdS-6 samples in 0.35 M Na₂S and 0.25 M Na₂SO₃; (b) Transient photocurrent response for CdS-1, CdS-2, CdS-3, CdS-4, CdS-5 and CdS-6 samples in 0.5 M Na₂SO₄; (c) Surface photovoltage spectra (SPV) of CdS-1 and CdS-5; (d) LSV curves for CdS-1 and CdS-5 samples in 1.0 M KOH with the scan rate was 5 mV s⁻¹.

agent beyond 20 days. Moreover, the new appeared peak at 164.03 eV relative to the S° in S 2p XPS spectra of used CdS-1 (Fig. S11a) further implies the severe photocorrosion happened during the irradiation process. Whereas, the S 2p XPS spectra of fresh and used CdS-5 (Fig. S11b) have no notable differences, further indicating its excellent photostability. This result indicates that CdS-5 can be used as a stable photocatalyst for boosting visible-light-driven H₂ production from water.

The electrochemical impedance spectroscopy (EIS) measurements were performed to explore the charge transfer and recombination process of the electrode materials in dark condition [42,43]. As shown in Fig. 8a, the arc radii of EIS Nyquist plots are gradually decreased with the molar ratio of S/Cd increasing. And the impedance of CdS-5 was much smaller than that of others samples, suggesting the self-constructed type-II {0001}/{10̄10} facet junctions can greatly improve the charge transfer and separation on CdS-5 single crystals.

The enhanced charge transfer and separation efficiency was further certified by the photocurrent-time responses of CdS photocatalyst. The photocurrent responses are generally employed to reveal the visible light photoelectrochemical performance occurring on the photocatalyst surface [43]. As shown in Fig. 8b, the transient photocurrent-time curves (*I* - *t* curves) were measured by several on-off cycles of intermittent irradiation under visible light ($\lambda \geq 420$ nm). The photocurrent intensity is more intensive with the S/Cd molar ratio increasing, which is consistent with the photocatalytic H₂ production activity. As expected, the facet-junction engineered CdS-5 produced the highest photocurrent density compared with that of other samples, whereas the lowest photocurrent density is observed in the CdS-1. The significantly enhanced photocurrent density of CdS-5 should be associated with the well-defined {0001}/{10̄10} facet junction and the surface sulfur vacancies, which accelerated the charge separation, transfer and surface reaction for more efficient photocatalytic H₂ production [33].

Surface photovoltage spectra (SPV) of CdS-1 and CdS-5 samples were investigated to further explore the separation and transfer

behaviors of the photo-excited charge carriers at the surface [44,45]. It has been reported that the SPV signal can be attributed to the variations of surface potential barriers during the light irradiation, which can identify the separation efficiency of photogenerated electrons and holes in surface [46,47]. As depicted in Fig. 8c, an obvious positive SPV response ranging from 300 to 600 nm can be observed for CdS-1 and CdS-5. This is representative feature of n-type semiconductor in SPV, where positive charges from inner semiconductor migrate to the surface [46]. Compared to CdS-1, the SPV response intensity of CdS-5 increases obviously, indicating that the photogenerated electron-hole pairs are separated more effectively [47]. The enhanced separation efficiency of electron-hole pairs can be attributed to the efficient charge transfer over the well-defined {0001}/{10̄10} facet junction and the surface sulfur vacancies in the CdS-5 sample. More importantly, the strongest SPV signal is consistent with the highest H₂ evolution rate, which can explain the origin of enhanced separation efficiency of photogenerated electron-hole pairs in the CdS-5 [47].

The electrochemical H₂ generation activities of CdS-1 and CdS-5 electrodes were also measured by the linear sweep voltammetry (LSV) method. As displayed in Fig. 8 d, the CdS-5 had a low overpotential of ~ -0.25 V vs. SCE compared with the CdS-1 (-0.36 V) at the current density of $-100 \mu\text{A cm}^{-2}$. This lower overpotential further confirming CdS-5 is an excellent photocatalyst for HER, because of the photocatalytic activity of HER is highly dependent on the overpotential of the HER reaction [48,49]. In a word, the CdS-5 with {0001}/{10̄10} facet junction significantly decreased the H₂-production overpotential.

On the basis of above results, the water splitting hydrogen evolution process of facet junction-engineered CdS-5 single crystals under visible-light irradiation ($\lambda \geq 420$ nm) is schematically illustrated in Fig. 9. Under visible light irradiation, the photogenerated electron on the {10̄10} facets of the CdS-5 single crystals will transfer to the CB of {0001} facets, while the produced holes on {0001} facets will transfer to the {10̄10} facets by the epitaxial interface of {0001} and {10̄10} facets. In a word, the photo-induced electrons and holes accumulated

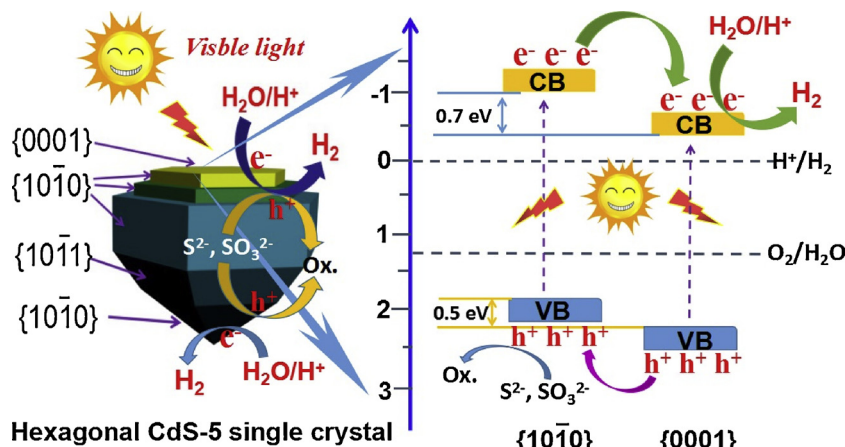


Fig. 9. Mechanism of photo-generated charge separation of the {0001}/{10̄0} facet junction over hexagonal CdS-5 single crystals for photocatalytic hydrogen evolution.

on the {0001} and {10̄0} facets, respectively. As a result, the electrons and holes of CdS-5 single crystals can be efficiently separated and the photocorrosion is effectively suppressed. As a consequence, a high stable and excellent photocatalytic activity are obtained over hexagonal CdS-5 single crystals. Three reasons may be responsible for the improved photocatalytic H₂ activity of the facet junction-engineered CdS-5: (1) the type-II band alignment between {0001} and {10̄0} facets results in a stable, longer life-time carriers due to spatial separation; (2) the epitaxial interface of {0001}/{10̄0} facet junction provides smooth channels for carrier transfer across the interface [33]; and (3) the good crystallinity and less crystal defects of CdS also can largely reduce the bulk electron-hole recombination.

4. Conclusions

In summary, we have for the first time synthesized a facet-junction hexagonal CdS single crystals with exposing {0001} and {10̄0} facets. The co-exposed {0001} and {10̄0} facets on hexagonal CdS single crystals with continuous band bending and well-defined epitaxial interfaces showed highly efficient visible-light-induced H₂ evolution. The maximum photocatalytic H₂ production rate of 24.33 mmol h⁻¹ g⁻¹ is obtained with an apparent quantum efficiency of 11.18% at 470 nm over the facet junction-engineered hexagonal CdS-5 single crystals, which is about 5.27 times greater than CdS-1 nanoparticles. And the superior photostability for H₂ evolution is also achieved, even after 25 consecutive cycles during 100 h light irradiation that impregnated in the strong alkaline sacrificial agent beyond 20 days, the initial photoactivity is still remained. The type-II band alignment between co-exposed {0001} and {10̄0} facets constructing facet junction with continuous band bending that significantly promoted the separation rate of photo-generated electrons and holes. Such a facet-mediated charge separation on hexagonal CdS single crystals by self-constructed {0001}/{10̄0} facet junction realized effective spatial charge separation. In addition, the small amount of sulfur vacancies are also benefit for the hydrogen evolution activity of CdS-5, which can largely reduce the bulk electron-hole recombination. The broadened absorption in the visible light region and lower over-potential are also responsible for the promoted photocatalytic hydrogen generation activity. This work represents a feasible and effective strategy for designing of facet-junction-engineered CdS single crystals with highly photocatalytic activity and unprecedented photostability.

Acknowledgments

This work was financially supported by NSFC (21773113, 21273106). The authors would like to thank Analysis Center of Nanjing

University for the sample characterization and the professor Guoqiang Li of Henan University for the SPV characterization.

Appendix A. Supplementary data

Supplementary material related to this article can be found, in the online version, at doi:<https://doi.org/10.1016/j.apcatb.2018.12.006>.

References

- [1] L. Cheng, Q.J. Xiang, Y.L. Liao, H.W. Zhang, CdS-based photocatalysts, *Energy Environ. Sci.* 11 (2018) 1362–1391.
- [2] K. Li, M. Han, R. Chen, S. Li, S. Xie, C. Mao, X. Bu, X. Cao, L. Dong, P. Feng, Y. Lan, Hexagonal@cubic CdS core@shell nanorod photocatalyst for highly active production of H₂ with unprecedented stability, *Adv. Mater.* 28 (2016) 8906–8911.
- [3] J. Zhang, S. Wageh, A. Al-Ghamdi, J. Yu, New understanding on the different photocatalytic activity of wurtzite and zinc-blende CdS, *Appl. Catal. B Environ.* 192 (2016) 101–107.
- [4] L. Shang, B. Tong, H. Yu, G.I.N. Waterhouse, C. Zhou, Y. Zhao, M. Tahir, L. Wu, C. Tung, T. Zhang, CdS nanoparticle-decorated Cd nanosheets for efficient visible light-driven photocatalytic hydrogen evolution, *Adv. Energy Mater.* 6 (2016) 1501241.
- [5] C. Zhu, C. Liu, Y. Zhou, Y. Fu, S. Guo, H. Li, S. Zhao, H. Huang, Y. Liu, Z. Kang, Carbon dots enhance the stability of CdS for visible-light-driven overall water splitting, *Appl. Catal. B Environ.* 216 (2017) 114–121.
- [6] F. Vaquero, R.M. Navarro, J.L.G. Fierro, Influence of the solvent on the structure, morphology and performance for H₂ evolution of CdS photocatalysts prepared by solvothermal method, *Appl. Catal. B Environ.* 203 (2017) 753–767.
- [7] J. Yu, Y. Yu, P. Zhou, W. Xiao, B. Cheng, Morphology-dependent photocatalytic H₂-production activity of CdS, *Appl. Catal. B Environ.* 156 (2014) 184–191.
- [8] N. Bao, L. Shen, T. Takata, K. Domon, Self-templated synthesis of nanoporous CdS nanostructures for highly efficient photocatalytic hydrogen production under visible light, *Chem. Mater.* 20 (2007) 110–117.
- [9] Q. Xiang, B. Cheng, J. Yu, Hierarchical porous CdS nanosheet-assembled flowers with enhanced visible-light photocatalytic H₂-production performance, *Appl. Catal. B Environ.* 138 (2013) 299–303.
- [10] J. Jin, J. Yu, G. Liu, P.K. Wong, Single crystal CdS nanowires with high visible-light photocatalytic H₂-production performance, *J. Mater. Chem. A* 1 (2013) 10927–10934.
- [11] C. Li, J. Yuan, B. Han, W. Shangguan, Synthesis and photochemical performance of morphology-controlled CdS photocatalysts for hydrogen evolution under visible light, *Int. J. Hydrogen Energy* 36 (2011) 4271–4279.
- [12] Y. Zhang, L. Han, C. Wang, W. Wang, T. Ling, J. Yang, C. Dong, F. Lin, X. Du, Zinc-blende CdS nanocubes with coordinated facets for photocatalytic water splitting, *ACS Catal.* 7 (2017) 1470–1477.
- [13] Y. Lu, X. Cheng, G. Tian, H. Zhao, L. He, J. Hu, S. Wu, Y. Dong, G. Chang, S. Lenaerts, S. Siffert, G.V. Tendeloo, Zhao. Li, L. Xu, X. Yang, B. Su, Hierarchical CdS/m-TiO₂/G ternary photocatalyst for highly active visible light-induced hydrogen production from water splitting with high stability, *Nano Energy* 47 (2018) 8–17.
- [14] Y. Hu, X. Gao, L. Yu, Y. Wang, J. Ning, S. Xu, X.W. Lou, Carbon-coated CdS petalous nanostructures with enhanced photostability and photocatalytic activity, *Angew. Chem. Int. Ed.* 52 (2013) 5636–5639.
- [15] B.J. Ma, H.J. Xu, K.Y. Lin, J. Li, H.J. Zhan, W.Y. Liu, C. Li, Mo₂C as Non-Noble Metal Co-Catalyst in Mo₂C/CdS Composite for Enhanced Photocatalytic H₂Evolution under Visible Light Irradiation, *ChemSusChem* 9 (2016) 820–824.
- [16] B.J. Ma, Y.H. Liu, J. Li, K.Y. Lin, W.Y. Liu, H.J. Zhan, Mo₂N: an efficient non-noble

- metal cocatalyst on CdS for enhanced photocatalytic H₂ evolution under visible light irradiation, *Int. J. Hydrogen Energy* 41 (2016) 22009–22016.
- [17] B.J. Ma, X.Y. Wang, K.Y. Lin, J. Li, Y.H. Liu, H.J. Zhan, W.Y. Liu, A novel ultra-efficient non-noble metal composite cocatalyst Mo₂N/Mo₂C/graphene for enhanced photocatalytic H₂ evolution, *Int. J. Hydrogen Energy* 42 (2017) 18977–18984.
- [18] Y.G. Chao, J.F. Zheng, H.X. Zhang, F. Li, F. Yan, Y.S. Tan, Z.P. Zhua, Oxygen-incorporation in Co₂P as a non-noble metal cocatalyst to enhance photocatalysis for reducing water to H₂ under visible light, *Chem. Eng. J.* 346 (2018) 281–288.
- [19] S. Bai, L. Wang, Z. Li, Y. Xiong, Facet-engineered surface and interface design of photocatalytic materials, *Adv. Sci.* 4 (2017) 1600216.
- [20] J. Pan, G. Liu, G. Lu, Cheng Hui, On the true photoreactivity order of {001}, {010}, and {101} facets of anatase TiO₂ crystals, *Angew. Chem.* 123 (2011) 2181–2185.
- [21] N. Zhang, C. Chen, Z. Mei, X. Liu, X. Qu, Y. Li, S. Li, W. Qi, Y. Zhang, J. Ye, V.A.L. Roy, R. Ma, Monoclinic tungsten oxide with {100} facet orientation and tuned electronic band structure for enhanced photocatalytic oxidations, *ACS Appl. Mater. Interfaces* 8 (2016) 10367–10374.
- [22] L. Bai, F. Ye, L. Li, J. Lu, S. Zhong, S. Bai, Facet engineered interface design of plasmonic metal and cocatalyst on BiOCl nanoplates for enhanced visible photocatalytic oxygen evolution, *Small* 13 (2017) 1701607.
- [23] X. Zhou, Z. Liu, Y. Wang, Y. Ding, Facet effect of Co₃O₄ nanocrystals on visible-light driven water oxidation, *Appl. Catal. B Environ.* 237 (2018) 74–84.
- [24] C. Zhen, C.Y. Jimmy, G. Liu, H.M. Cheng, Selective deposition of redox co-catalyst (s) to improve the photocatalytic activity of single-domain ferroelectric PbTiO₃ nanoplates, *Chem. Commun.* 50 (2014) 10416–10419.
- [25] S. Song, Z. Liang, W. Fu, T. Peng, Preparation of single-crystalline AgIn₅S₈ octahedrons with exposed {111} facets and its visible-light-Responsive photocatalytic H₂ production activity, *ACS Appl. Mater. Interfaces* 9 (2017) 17013–17023.
- [26] R. Li, F. Zhang, D. Wang, J. Yang, M. Li, J. Zhu, X. Zhou, H. Han, C. Li, Spatial separation of photogenerated electrons and holes among {010} and {110} crystal facets of BiVO₄, *Nat. Commun.* 4 (2013) 1432.
- [27] B. Wang, S. Shen, L. Guo, Surface reconstruction of facet-functionalized SrTiO₃ nanocrystals for photocatalytic hydrogen evolution, *ChemCatChem* 8 (2016) 798–804.
- [28] X. Yin, X. Li, H. Liu, W. Gu, W. Zou, L. Zhu, Z. Fu, Y. Lu, Realizing selective water splitting hydrogen/oxygen evolution on ferroelectric Bi₃TiNbO₉ nanosheets, *Nano Energy* 49 (2018) 489–497.
- [29] J. Yu, J. Low, W. Xiao, P. Zhou, M. Jaroniec, Enhanced photocatalytic CO₂-reduction activity of anatase TiO₂ by coexposed {001} and {101} facets, *J. Am. Chem. Soc.* 136 (2014) 8839–8842.
- [30] L. Liu, Y. Jiang, H. Zhao, J. Chen, J. Cheng, K. Yang, Y. Li, Engineering co-exposed {001} and {101} facets in oxygen-deficient TiO₂ nanocrystals for enhanced CO₂ photoreduction under visible light, *ACS Catal.* 6 (2016) 1097–1108.
- [31] Y. Cao, Q. Li, C. Li, J. Li, J. Yang, Surface heterojunction between (001) and (101) facets of ultrafine anatase TiO₂, nanocrystals for highly efficient photoreduction CO₂ to CH₄, *Appl. Catal. B Environ.* 198 (2016) 378–388.
- [32] B.J. Ma, K.Y. Lin, W.G. Su, W.Y. Liu, One-pot synthesis of ZnO/ZnGa₂O₄ heterojunction with X/X'Y structure for improved photocatalytic activity, *Appl. Surf. Sci.* 317 (2014) 682–687.
- [33] A. Zhang, W. Wang, J. Chen, C. Liu, Q. Li, X. Zhang, W. Li, Y. Si, H. Yu, Epitaxial facet junctions on TiO₂ single crystals for efficient photocatalytic water splitting, *Energy Environ. Sci.* 11 (2018) 1444–1448.
- [34] C. Li, L. Han, R. Liu, H. Li, S. Zhang, G. Zhang, Controlled synthesis of CdS micro/nano leaves with (0001) facets exposed: enhanced photocatalytic activity toward hydrogen evolution, *J. Mater. Chem.* 22 (2012) 23815–23820.
- [35] X. Wang, M. Liu, Z. Zhou, L. Guo, Toward facet engineering of CdS nanocrystals and their shape-dependent photocatalytic activities, *J. Phys. Chem. C* 119 (2015) 20555–20560.
- [36] Y. Xiong, J. Zhang, F. Huang, G. Ren, W. Liu, D. Li, C. Wang, Z. Lin, Growth and phase-transformation mechanisms of nanocrystalline CdS in Na₂S solution, *J. Phys. Chem. C* 112 (2008) 9229–9233.
- [37] F. Kurnia, Y.H. Ng, R. Amal, N. Valanoor, J.N. Hart, Defect engineering of ZnS thin films for photoelectrochemical water-splitting under visible light, *Sol. Energy Mater. Sol. Cells* 153 (2016) 179–185.
- [38] X. Hao, Y. Wang, J. Zhou, Z. Cui, Y. Wang, Z. Zou, Zinc vacancy-promoted photocatalytic activity and photostability of ZnS for efficient visible-light-driven hydrogen evolution, *Appl. Catal. B Environ.* 221 (2018) 302–311.
- [39] S. Yi, J. Yan, B.R. Wulan, S. Li, K. Liu, Q. Jiang, Noble-metal-free cobalt phosphide modified carbon nitride: an efficient photocatalyst for hydrogen generation, *Appl. Catal. B Environ.* 200 (2017) 477–483.
- [40] L. Huang, J. Yang, X. Wang, J. Han, H. Han, C. Li, Effects of surface modification on photocatalytic activity of CdS nanocrystals studied by photoluminescence spectroscopy, *Phys. Chem. Chem. Phys.* 15 (2013) 553–560.
- [41] L. Yang, J. Huang, L. Shi, L. Cao, Q. Yu, Y. Jie, J. Fei, H. Ouyang, J. Ye, A surface modification resultant thermally oxidized porous g-C₃N₄ with enhanced photocatalytic hydrogen production, *Appl. Catal. B Environ.* 204 (2017) 335–345.
- [42] G. Ai, H. Li, S. Liu, R. Mo, J. Zhong, Solar water splitting by TiO₂/CdS/Co-Pi nanowire array photoanode enhanced with Co-Pi as hole transfer relay and CdS as light absorber, *Adv. Funct. Mater.* 25 (2015) 5706–5713.
- [43] J. Wen, J. Xie, H. Zhang, A. Zhang, Y. Liu, X. Chen, X. Li, Constructing multi-functional metallic Ni interface layers in the g-C₃N₄ nanosheets/amorphous NiS heterojunctions for efficient photocatalytic H₂ generation, *ACS Appl. Mater. Interfaces* 9 (2017) 14031–14042.
- [44] X. Yue, S. Yi, R. Wang, Z. Zhang, S. Qiu, A novel and highly efficient earth-abundant Cu₃P with TiO₂ “P–N” heterojunction nanophotocatalyst for hydrogen evolution from water, *Nanoscale* 8 (2016) 17516–17523.
- [45] H. Chen, F. Zhang, X. Sun, W. Zhang, G. Li, Effect of reaction atmosphere on photodeposition of Pt nanoparticles and photocatalytic hydrogen evolution from SrTiO₃ suspension system, *Int. J. Hydrogen Energy* 43 (2018) 5331–5336.
- [46] L. Bi, D. Xu, L. Zhang, Y. Lin, D. Wang, T. Xie, Metal Ni-loaded g-C₃N₄ for enhanced photocatalytic H₂ evolution activity: the change in surface band bending, *Phys. Chem. Chem. Phys.* 17 (2015) 29899–29905.
- [47] C. Han, L. Wu, L. Ge, Y. Li, Z. Zhao, AuPd bimetallic nanoparticles decorated graphitic carbon nitride for highly efficient reduction of water to H₂ under visible light irradiation, *Carbon* 92 (2015) 31–40.
- [48] X. Hao, Z. Cui, J. Zhou, Y. Wang, Y. Hu, Y. Wang, Z. Zou, Architecture of high efficient zinc vacancy mediated Z-scheme photocatalyst from metal-organic frameworks, *Nano Energy* 52 (2018) 105–116.
- [49] W. Zhen, X. Ning, B. Yang, Y. Wu, Z. Li, G. Lu, The enhancement of CdS photocatalytic activity for water splitting via anti-photocorrosion by coating Ni₂P shell and removing nascent formed oxygen with artificial gill, *Appl. Catal. B Environ.* 221 (2018) 243–257.